11th AIAA/CEAS Aeroacoustics Conference, 23-25 May 2005, Monterey, California

An investigation of outlet boundary conditions for incompressible near field acoustics

Jonas Ask *

Volvo Car Corporation, Fluid Dynamic Center SE-405 31 Göteborg, Sweden

and Lars Davidson †

Chalmers University of Technology, SE-412 96 Göteborg, Sweden

The aim with this study is primarily to investigate different outlet boundary conditions and their effect on the background pressure when strong vortices are present in the domain. These vortices can cause local back flow to occur over the outlet causing numerical problems and erroneous results. Generally this can be avoided by improving the outlet boundary condition, increase the mesh stretching, extending the domain far downstream or to introduce artificial dissipation through buffer-zones or so called fringe layers. This is crucial for incompressible methods since pressure distortions caused by the outlet is spread instantaneously in the domain and will pollute the dipole terms in the Lighthill-Curle's analogy [1]. In this work three different formulations of an outlet boundary condition are evaluated followed by an investigation of a buffer-zone technique for a first test case. This first case is a convected clock wise rotating vortex over a wall superimposed to a laminar velocity profile. The findings indicate that the outlet boundary condition cannot alone prevent reflections to occur when a strong vortex is convected over the outlet. The results from the buffer-zone evaluation show that this technique can successfully be used also for incompressible simulations. However, as for compressible simulations a sufficient damping region is crucial for eliminating the reflections caused by the outlet. Two critical parameters are identified, namely the vortex intensity and the length of the buffer-zone. The findings from this part is then used in a second case where the final goal is to evaluate the emitted sound. This second case is an open two dimensional cavity with a laminar upstream boundary layer. Additionally, a second order central scheme is compared against the monotonic second order Van Leer scheme [2]. As expected the upwind scheme is more dissipative than the central scheme. This result in generally higher vortex intensity levels when the central scheme is used.

The sound radiation and propagation in the open cavity case is then found by evaluating the near and far field dipole terms in a time integral solution of Lighthill-Curle's analogy. The results are compared against previously published compressible simulations at the corresponding Mach number of 0.15 [3, 4]. It is shown that both wall source intensities and sound directivity are well predicted with this methodology.

Nomenclature

Latin symbols

*PhD student

†Professor, Division of Fluid Dynamics, Department of Applied Mechanics

a	speed of sound
C_d	drag coefficient
C_p	pressure coefficient
c	pseudo-sound of speed
D	cavity depth
f	frequency
I	intensity
L	cavity length
l_i	unit vector pointing from source to observer
n_i	unit surface normal
p	pressure
r	radial distance
S	integration surface
T_{ij}	Lighthill stress tensor
t	time
u_i	instantaneous velocity
U	mean stream-wise velocity
v_t	tangential velocity
V	integration volume
$\mathbf{x}$	observer coordinates
x_i	cartesian tensor coordinate
$\mathbf{y}$	source coordinates

Greek symbols

δ_{ij}	Kronecker delta
ρ	density
Ω	vorticity
σ	buffer strength
τ_{ij}	viscous stress tensor
ϕ	source term

Subscripts

0	reference state
c	bulk condition
l	index
$init$	initial condition
max	maximum value
min	minimum value
rms	root-mean-square
w	wall condition
∞	ambient

Superscripts

$\cdot$	temporal derivative
$\prime$	fluctuation
$\imath$	shape parameter
l	local value

Abbreviations

CFL	Courant-Friedrichs-Lewy
DNS	Direct-Numerical-Simulation
$SIMPLEC$	Semi-Implicit Method for Pressure-Linked Equations-Consistent

I. Introduction

Cavity flows have been the subject of extensive research during many years. In [5] self-sustained oscillations occurring in cavity flows can be categorized into *Fluid-dynamic*, *Fluid-resonant* and *Fluid-elastic* oscillations depending on the dominating cause. Oscillations of the *Fluid-dynamic* type were in [6] further divided into *Self-sustained* oscillation modes and *Wake mode* due to an abrupt cavity drag increase above a critical width-to-depth ratio. A numerical study was conducted in [7] where compressible simulations for both *Wake-mode* and *Shear-layer mode* flow regimes were carried out for laminar upstream flows. Further insight in the mode or regime shift of open cavities was presented in [8] where simulations were conducted as parameter studies of Mach number, boundary layer thickness and length-to-depth ratio. In [3, 4] compressible simulations were conducted for an open cavity oscillating in *Wake-mode*. A comparison was made of directly computed noise with the corresponding results computed by an acoustic analogy. A further study for the same case was conducted in [9] in an attempt to find the noise generation and propagation by an incompressible approach. A parameter study was here conducted of different time step sizes and domain sizes based on second order schemes and an outlet boundary condition of *convective* type.

Buffer-zones for incompressible simulations was investigated in [10] with focus on the length and strength of the buffer-zone. This paper is a further attempt to find the emitted noise from an incompressible simulation by the use of this technique. The flow regime oscillates in *Wake-mode* which implies that an incompressible approach is feasible and the simulations corresponds to the work made by [3, 4].

In compressible simulations the time step size is limited by the local sound wave propagation and the flow convective speed. For low Mach number wall bounded flows the limiting time step parameter is the sound wave propagation. This makes the incompressible assumption an attractive approach for Mach number below typically 0.3. In this work this approach is investigated and its effect on the radiated sound by the use of an acoustic analogy. For this purpose a time integral solution to Lighthill-Curle's equation is used to extract sources from the incompressible flow field. This is a common approach and has been the subject of extensive research during the last years. The method is based on a two step procedure for evaluating the sound pressure level at an observer point. In this paper the near and far field pressure terms are used to obtain the radiated sound. These terms have been identified as the two dominating terms for the open cavity case [3, 4].

When strong vortices exist in the domain local back flow and high gradients can exist over the outlet. This can be avoided by extending the domain far downstream until the vortex is dissipated by the viscosity. Another way is to increase the mesh stretching and thus introducing additional numerical dissipation or to add a dissipative source term so that the flow fulfills an artificial Dirichlet boundary condition. A fourth alternative is to use a softer boundary condition at the outlet. The first of the above alternatives is the most straight forward way but requires a large amount of cells due to an increased domain length. Introducing numerical dissipation through buffer-zones is easily implemented and makes the damping ratio more controllable compared to an excessive mesh stretching. Improving the boundary condition is the most attractive way and requires least amount of cells of the above alternatives but is mathematically and numerically hard to find and implement. In this work the use of buffer-zones for incompressible simulations is implemented and evaluated as well as an evaluation of three different outlet boundary conditions.

II. Methodology

This chapter is divided into four subsections. The first section describes the solver and the numerical schemes to find the flow field. The second section contains the derivation of the different outlet boundary conditions. The third treats the buffer-zone technique and the fourth presents the acoustic analogy used in the second open cavity case.

A. The Finite Volume Solver

The solver used for this purpose is the incompressible collocated finite volume code CALC-BFC [11]. Versions of this code has successfully been used by [12–15], for various applications. The discretization scheme in time is the semi-implicit Crank-Nickolson time marching scheme. The pressure is coupled to the velocity field through the SIMPLEC pressure-velocity correction algorithm and the computational mesh is based on a single block arrangement. For the convective fluxes two different schemes are used for evaluation, the second order central scheme and the monotonic second order Van Leer scheme [2]. All simulations conducted in this paper are considered laminar and two dimensional.

B. The outlet boundary condition

The Euler equations in two dimensions and the continuity equation written on a pseudo-compressible form state

$$\frac{\partial P}{\partial t} + c^2 \frac{\partial u_1}{\partial x_1} + c^2 \frac{\partial u_2}{\partial x_2} = 0 \tag{1}$$

$$\frac{\partial u_1}{\partial t} + \frac{\partial}{\partial x_1}(u_1^2 + P) + \frac{\partial}{\partial x_2}(u_1 u_2) = 0 \tag{2}$$

$$\frac{\partial u_2}{\partial t} + \frac{\partial}{\partial x_1}(u_1 u_2) + \frac{\partial}{\partial x_2}(u_2^2 + P) = 0 \tag{3}$$

In Eqs. 1 to 3, $P = \frac{p}{\rho}$, according to the notation used in [16] and c represent the pseudo-sound of speed. In the limit of an infinite pseudo-sound speed Eq. 1 turns into the incompressible continuity equation and it is in this limit the analysis is evaluated. The two flux vectors E and F can then be identified as

$$E = \begin{pmatrix} c^2 u_1 \\ u_1^2 + P \\ u_1 u_2 \end{pmatrix}, \quad F = \begin{pmatrix} c^2 u_2 \\ u_1 u_2 \\ u_2^2 + P \end{pmatrix} \tag{4}$$

These set of equations can be written on a quasi-linear form at the reference solution q_0

$$\frac{\partial q'}{\partial t} + \boldsymbol{A}_0 \frac{\partial q'}{\partial x_1} + \boldsymbol{B}_0 \frac{\partial q'}{\partial x_2} = 0 \tag{5}$$

where

$$q' = \begin{pmatrix} P \\ u_1 \\ u_2 \end{pmatrix}, \quad \boldsymbol{A}_0 = \left(\frac{\partial E}{\partial q}\right)_0 = \begin{pmatrix} 0 & c^2 & 0 \\ 1 & 2u_1 & 0 \\ 0 & u_2 & u_1 \end{pmatrix}, \quad \boldsymbol{B}_0 = \left(\frac{\partial F}{\partial q}\right)_0 = \begin{pmatrix} 0 & 0 & c^2 \\ 0 & u_2 & u_1 \\ 1 & 0 & 2u_2 \end{pmatrix} \tag{6}$$

and $\boldsymbol{A}_0$ and $\boldsymbol{B}_0$ in Eq. 6 are the flux Jacobian matrices evaluated at the reference solution. If one assumes that the perturbations correspond to planar waves aligned with the unit vector $n_i = \boldsymbol{n} = (\alpha_1, \alpha_2)$, Eq. 5 can be rewritten as

$$\frac{\partial q'}{\partial t} + \widetilde{\boldsymbol{A}}_0 \frac{\partial q'}{\partial \xi} = 0 \tag{7}$$

where

$$\widetilde{\boldsymbol{A}}_0 = \alpha_1 \left(\frac{\partial E}{\partial q}\right)_0 + \alpha_2 \left(\frac{\partial F}{\partial q}\right)_0 = \begin{pmatrix} 0 & \alpha_1 c^2 & \alpha_2 c^2 \\ \alpha_1 & 2\alpha_1 u_1 + \alpha_2 u_2 & \alpha_2 u_1 \\ \alpha_2 & \alpha_1 u_2 & \alpha_1 u_1 + 2\alpha_2 u_2 \end{pmatrix} \tag{8}$$

and $\xi = n_i x_i$. Equation 7 is thus a coupled system of equations describing the propagation of a planar wave in the ξ direction. Matrices $\boldsymbol{T}$ and $\boldsymbol{T}^{-1}$ can then be found analytically so that $\widetilde{\boldsymbol{A}}_0$ is diagonalized

$$\boldsymbol{T}\widetilde{\boldsymbol{A}}_0\boldsymbol{T}^{-1} = \boldsymbol{\Lambda} = \begin{pmatrix} \lambda_1 & 0 & 0 \\ 0 & \lambda_2 & 0 \\ 0 & 0 & \lambda_3 \end{pmatrix}, \quad \boldsymbol{T} = \big((T_1)\,(T_2)\,(T_3)\big) \tag{9}$$

where T_i are the eigenvectors of $\widetilde{\boldsymbol{A}}_0$. The eigenvalues $\lambda_1, \lambda_2, \lambda_3$ can be found analytically in the limit of an infinite pseudo-sound speed as

$$\begin{aligned} \lambda_1 &= \alpha_1 u_1 + \alpha_2 u_2 \\ \lambda_2 &= +\infty \\ \lambda_3 &= -\infty \end{aligned} \tag{10}$$

In Eq. 10, λ_1 corresponds to a vorticity wave and the two other eigenvalues, λ_2 and λ_3 represent a positive and negative pseudo-sound wave propagating at infinite speed respectively. The characteristic variables can then be defined as

$$W = \boldsymbol{T}^{-1} q' \tag{11}$$

where the only finite variable in W is

$$W_1 = \frac{\alpha_2 u_1 + \alpha_1 u_2}{\sqrt{\alpha_1^2 + \alpha_2^2}} \tag{12}$$

Equation 7 can then be decoupled through a transport equation for the characteristic variables

$$\frac{\partial W}{\partial t} + \Lambda \frac{\partial W}{\partial \xi} = 0 \tag{13}$$

The resulting characteristic variable in the limit of infinite propagation speed and a boundary whose normal vector is aligned with the α_1 direction is

$$W_1 = u_2 \tag{14}$$

The overall conclusion from the above analysis is that a boundary condition on the form

$$\frac{\partial u_2}{\partial t} + u_c \frac{\partial u_2}{\partial x_1} = 0 \tag{15}$$

where $u_c = u_1$ is a proper non-reflective boundary condition for planar vorticity waves propagating normal to α_1. Strictly speaking u_1 is a part of the solution and there is only a transport equation for u_2. However, in the incompressible LES community [12, 14], it is common to apply a transport equation for both u_1 and u_2 where the convection velocity is the freestream or the bulk velocity $u_c = U_c$. This boundary condition is often referred to as a *convective boundary condition*. When the flow is bounded by a wall at the outlet the mean convection velocity approaches zero and if a freestream condition ($u_c = U_c$) is applied it can result in reflections as well as phase errors of the convected disturbances. This traditionally used outlet boundary condition can be improved by instead using a local time averaged ($u_c = U_l$) or otherwise known local velocity. The evaluated formulations used in this paper are presented in Eqs. 16 to 18.

$$\frac{\partial \boldsymbol{u_i}}{\partial t} + U_c \frac{\partial \boldsymbol{u_i}}{\partial \boldsymbol{x_j}} = 0 \tag{16}$$

$$\frac{\partial \boldsymbol{u_i}}{\partial t} + U_l \frac{\partial \boldsymbol{u_i}}{\partial \boldsymbol{x_j}} = 0 \tag{17}$$

$$\frac{\partial \boldsymbol{u_i}}{\partial t} + u_1 \frac{\partial \boldsymbol{u_i}}{\partial \boldsymbol{x_j}} = 0 \tag{18}$$

Equation 16 uses a globally defined freestream or bulk velocity, U_c. Equation 17 uses a local time averaged or otherwise known local steady-state velocity, U_l and Eq. 18 uses the instantaneous local streamwise velocity, u_1.

C. The buffer-zone technique

In this section a buffer-zone technique is presented to prevent reflections to occur when strong vortices are convected over the outlet. The method is commonly used for compressible simulations when flow induced noise is of interest. Buffer-zones are for this purpose introduced to prevent sound waves from being reflected back into the domain and contaminate the solution. The advantage in compressible simulations is that the sound waves can be damped over the buffer-zone both when propagating toward the outlet and when they are reflected back into the domain at the outlet.

In incompressible simulations no sound waves are present and the purpose with the buffer-zone in this context is to dissipate the vorticity by forcing the velocities to reach a defined target level. The damping term used in the following text is defined as

$$\sigma \left[\frac{x_1 - x_{1,min}}{x_{1,max} - x_{1,min}} \right]^i \left(u_i - u_i^{target} \right) \tag{19}$$

where i is a shape parameter. The amplification parameter σ is chosen on dimensional grounds, in this case to 1.0 s^{-1} and u_i^{target} are the target velocity. The target velocity should ideally be defined as the local time average velocity which would require the least amount of damping. The source term Eq. 19 is further divided into a constant and a linear part and added to the governing equations. Another intention with this study is to find a relation between spatially integrated vortex intensity and the required length of the buffer-zone for a fixed buffer-zone shape and a mean vortex convection speed. To evaluate this intensity the vorticity over the buffer-zone entrance plane is first computed as

$$\Omega_z = \frac{\partial u_2}{\partial x_1} - \frac{\partial u_1}{\partial x_2} \tag{20}$$

The vortex intensity is then computed as

$$I_\omega = \frac{\int_0^H (\Omega_z^{rms}) dx_2}{H} \tag{21}$$

D. The acoustic analogy

When computing the near field acoustics of a flow the most straight forward method is to conduct a compressible DNS (Direct Numerical Simulation). With this approach it is possible to directly measure sound emissions at any position in the computational domain. If one instead is interested in finding the emissions at a point outside the computational domain a different strategy must be used. For flows where walls are present a feasible way is to use either Ffowkes-Williams and Hawkings or Curle's analogy [1, 17]. For steady and impermeable integration surfaces these two analogies are identical. Two major assumptions are made in these analogies. The density fluctuations which is the dependent variable exists on both side of the equation and thus decouples the sound wave operator from the sources. This is a reasonable assumption for low Mach number flows where sound emissions are primarily caused by the hydrodynamics. The next assumption is that only isotropic wave propagation is taken into consideration which is only true for flow with zero mean motion. A modified version of Lighthill-Curle's equation is used in this work with temporal derivatives inside the integral instead of keeping the spatial derivatives outside the integral as Curle's [1] original formulation states. The derivation can be found in [3] and corresponds to *Formulation 1A* in [18] for the conditions mentioned above.

$$p(\mathbf{x},t) - p_\infty = \frac{1}{4\pi} \int_V \left[\frac{l_i l_j}{a_\infty^2 r} \ddot{T}_{ij} + \frac{3l_i l_j - \delta_{ij}}{a_\infty r^2} \dot{T}_{ij} + \frac{3l_i l_j - \delta_{ij}}{r^3} T_{ij} \right] dV(\mathbf{y}) + \frac{1}{4\pi} \int_S l_i n_j \left[\frac{\dot{p}\delta_{ij} - \dot{\tau}_{ij}}{a_\infty r} + \frac{p\delta_{ij} - \tau_{ij}}{r^2} \right] dS(\mathbf{y}) \tag{22}$$

Equation 22 is valid for three dimensions while the flow field is computed in two dimensions. Thus, the solution is expanded in the spanwise direction. A sensitivity study of this expansion was conducted in [3, 4]. In the following text, source term 1 and 2 will refer to the wall pressure and the time derivative of the wall pressure respectively, which are the only terms treated in this work.

III. Description of the cases

Two cases are presented in this paper. The first case is a two dimensional vortex convected downstream by an upstream laminar profile and will be denoted as the *Test case*. This case will be used for both the boundary condition study as well as the buffer layer study. The second case is an open cavity with an upstream laminar profile with a length-to-depth ratio of $L/D = 4$. This case will be denoted as the *Open cavity case*.

A. The test case

The computational domain is bounded by an inlet at $x_1 = -4.3$ and an outlet at $x_1 = 14.0$. The upper boundary is placed at $x_2 = 11.0$ and the lower boundary is positioned at $x_2 = 0.0$. A visual representation of the domain can be found in Fig. 2. As the overall goal with this case is to calibrate parameters and evaluate boundary conditions for the open cavity case similar geometrical dimensions are used. The freestream velocity is $U_\infty = 1.0$ and the Reynolds number is $Re = 1500$. The density $\rho = 1.0$ which gives a viscosity of $\mu = 1/1500$. The chosen Reynolds number is the same as for the open cavity case and is based on a characteristic unit length. The initial disturbance is defined as

$$v_t(x_1, x_2) = -\beta r^2 \exp[-\alpha r^2] \tag{23}$$

where $r = \sqrt{(x_1 - x_{1,init})^2 + (x_2 - x_{2,init})^2}$, $\beta = 6$ and $\alpha = 2$. The disturbance is initiated at $x_{1,init} = 2.333$ and $x_{2,init} = 1.666$ and is superimposed to a laminar velocity profile shown in Fig. 1. The incoming laminar boundary layer is identical to the profiles used in the open cavity case and is extracted from the compressible reference case, explained in the following chapter. Its virtual origin is located at $x_1 \approx -5.93$.

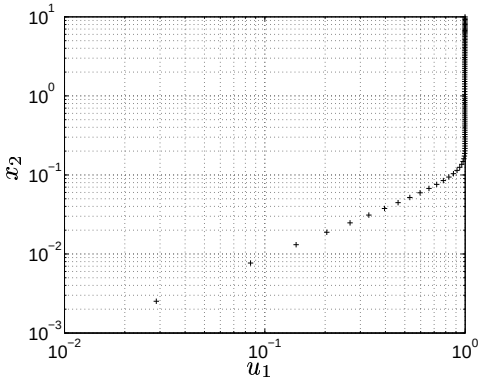

Figure 1. Inlet u_1 profile

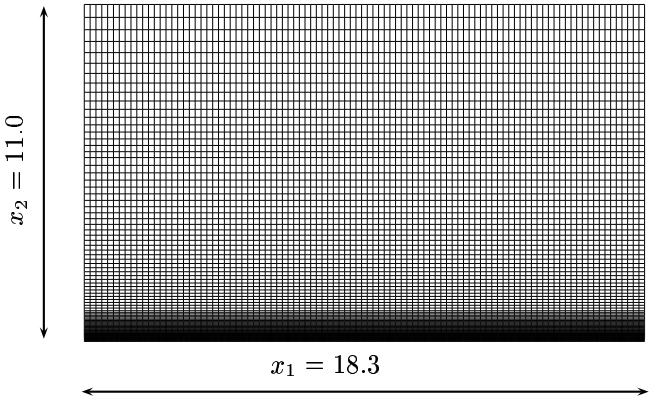

Figure 2. Test case geometry and mesh

The following boundary conditions are used for the test case:

- $\boldsymbol{u_i} = 0$ at the lower boundary
- Symmetry at the upper boundary
- $\boldsymbol{u_i}$ profiles over the inlet according to the reference case

- Outlet boundary condition as described in Table 1.

The time step size used for the test case is $\Delta t = 0.05$ which corresponds to a maximum CFL number of $CFL_{max} \approx 0.3$.

B. The open cavity case

The second case is the flow over an open cavity with a length-to-depth ratio of $L/D = 4$. The incompressible results are compared with the compressible simulation conducted at a Mach number of 0.15 and the compressible simulation will in the further text be referred to as the *Reference case*. Regarding the reference case more information about methodology, boundary conditions and discretization schemes can be found in [3, 4]. An overview of the computational domain is presented in Fig. 3. The following boundary conditions

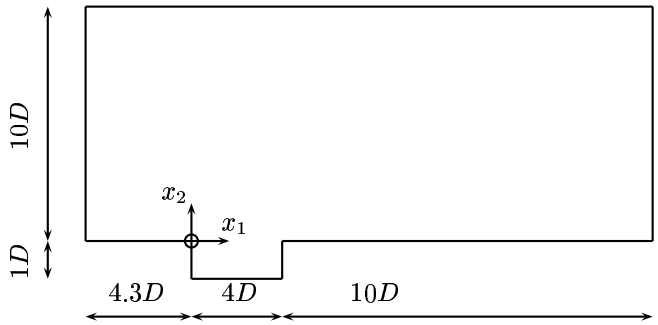

Figure 3. Geometrical dimensions for the open cavity case

are used for this case

- $\boldsymbol{u_i} = 0$ at the walls
- Symmetry at the upper boundary
- $\boldsymbol{u_i}$ profiles over the inlet according to the reference case
- Buffer-zone entrance plane at $x_1 = 14.0$

The Reynolds number is $Re_D = 1500$ based on the cavity depth. A time step of $\Delta t = 0.005$ results in a maximum CFL number of 0.5 close to the trailing edge of the cavity. This time step was used in all the presented open cavity simulations. The resolution in the cavity is approximately 80 cells per unit length in both directions. The domain is resolved by 900 nodes in the streamwise direction and 250 nodes in the flow normal direction. In the streamwise direction the node distribution is 250 nodes over the inlet to the cavity leading edge wall, 250 nodes over the cavity bottom wall and 400 nodes over the cavity trailing edge to the outlet. The wall extending from the inlet to the cavity leading edge is referred to as the *inlet wall* and the wall extending from the cavity trailing edge to the buffer-zone entrance plane is referred to as the *outlet wall*.

IV. Results from the test case

First part of this section presents the results from boundary condition evaluation followed by the buffer-zone study. A summary of the different cases are presented in Table 1 where VL is the Van Leer scheme

Boundary condition study		
Case	BC	Discretization scheme
BC1	Eq.(16)	VL
BC2	Eq.(16)	C
BC3	Eq.(17)	VL
BC4	Eq.(17)	C
BC5	Eq.(18)	VL

Table 1. Boundary conditions and discretization schemes

and C is the central scheme. In Figs. 4(a) and 4(c) the wall pressure intensities for the different cases are presented along the lower boundary extending from the inlet to the outlet. The wall pressure intensity is defined as

$$I = 20log_{10}\left(\frac{p_w^{rms}}{p_{ref}}\right), \qquad p_{ref} = \sqrt{\rho_\infty a_\infty 10^{-12}} \tag{24}$$

where $a_\infty = 1/0.15$, according to the open cavity case. Generally the intensities increase for all cases when approaching the outlet. Highest levels close to the outlet can be found for BC5 although this case is carried out with the upwind scheme. The central scheme used in BC2 and BC4 also show high intensities in this region as expected for an unbounded scheme. It appears that the test case is insensitive to whether the convection speed is defined as the freestream velocity or a local steady-state velocity. Convection velocity based on a local average velocity ($u_c = U_l$) should give more accurate results if the vortices are located closer to the wall. Further more, the reasons for the high outlet intensities can be explained when studying the time signal of the wall pressure at $x_1 = 4.211$ in Figs. 4(b) and 4(d). The vortex reaches the outlet at $t \approx 11.7$ based on the freestream velocity and the distance between the vortex initial position and the outlet. Indeed all the cases show a symmetric pressure distortion for $t \approx 11.7$. Although the monitoring point is located $x_1 \approx 9.8$ from the outlet high pressure oscillations are found at the time the vortex is convected over the outlet. From these findings it appears that outlet boundary conditions of the type presented above are not well suited for the kind of flow present in the test case. This leads us to the buffer-zone investigation.

The investigated cases for the buffer-zone study are presented in Table 2. In Table 2, NC and XB are

Buffer parameter study				
Case	NC/XB	Discretization scheme	Shape parameter(i)	I_ω
B1	20/3.657	C	2	0.167
B2	20/3.657	VL	2	0.145
B3	40/7.310	C	2	0.163
B4	40/7.310	VL	2	0.142
B5	40/7.310	C	1	0.167
B6	40/7.310	VL	1	0.144

Table 2. Buffer parameters and discretization schemes

the number of cells in the x_1 direction and the length of the buffer-zone, respectively. The vortex intensity

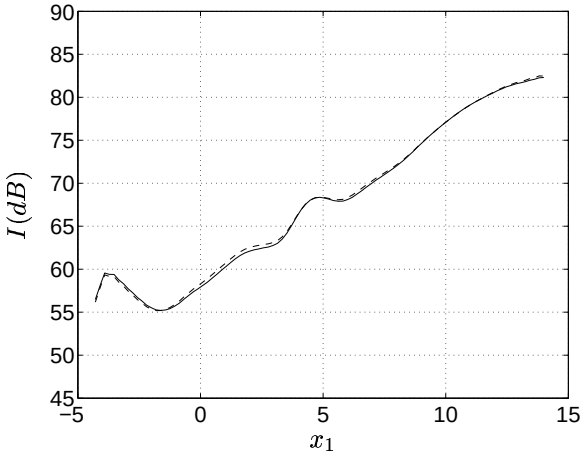

(a) Wall pressure intensities for the central schemed cases BC2 (−), BC4 (−−)

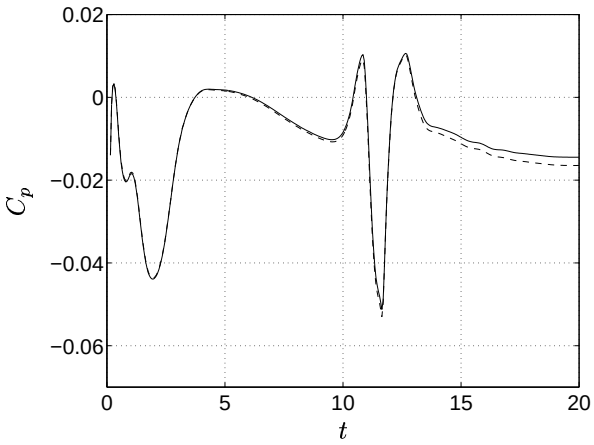

(b) Time series of C_p at $x_1 = 4.211$, $x_2 = 0$ for the central schemed cases BC2 (−), BC4 (−−)

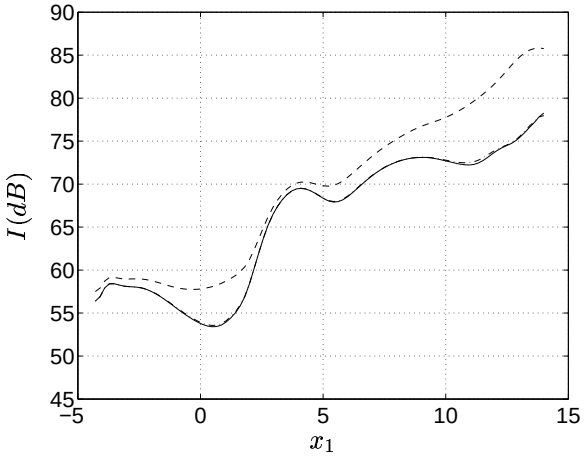

(c) Wall pressure intensities for the upwind schemed cases BC1 (−), BC3 (−.), BC5 (−−)

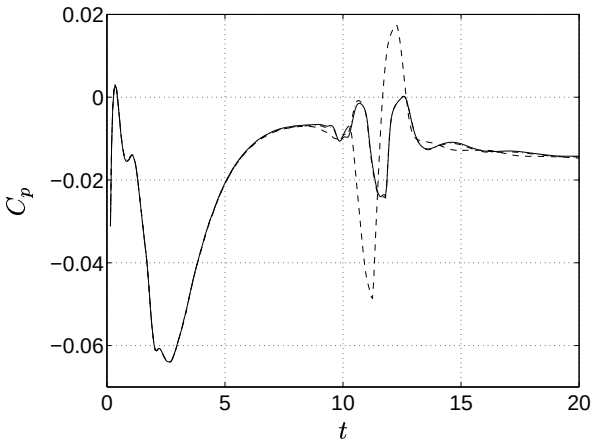

(d) Time series of C_p at $x_1 = 4.211$, $x_2 = 0$ for the upwind schemed cases BC1 (−), BC3 (−.), BC5 (−−)

Figure 4. Results from the outlet boundary condition evaluation according to Table 1

is also included. The findings indicate that the central scheme gives generally higher vortex intensity over the buffer-zone entrance plane compared to the upwind cases. Additional results from the buffer-zone study are presented in Figs. 5(a) to 5(d).

Figures 5(a) and 5(c) show the rms values of the pressure along the lower wall from the inlet to the buffer-zone entrance plane. If a comparison is made against Figs. 4(a) and 4(c) the intensities are significantly lower which indicates that the buffer-zone works as intended. The time signals of the wall pressure is also presented in Figs. 5(d) and 5(b). The vortex enters and leaves the buffer-zone later in time compared to the boundary condition study due to the extended domains. The corresponding time-intervals are $11.67 < t < 15.32$ for cases B1 and B2 and $11.67 < t < 18.98$ for cases B3 to B6. Promising results are found for cases B3 and

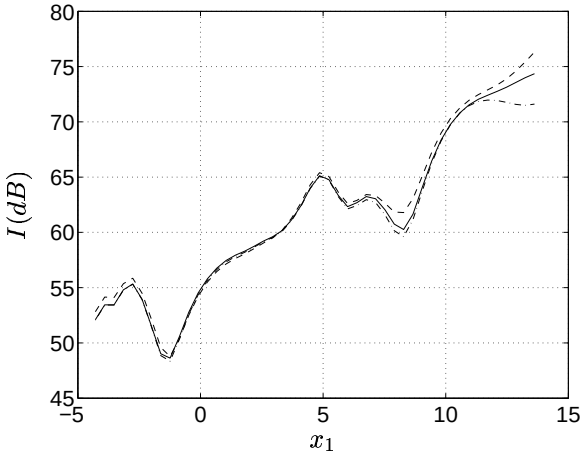

(a) Wall pressure intensities for the central schemed cases B1 (−−), B3 (−.), B5 (−)

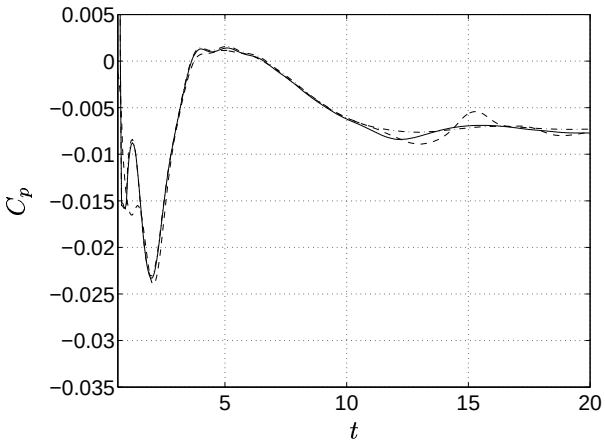

(b) Time series of C_p at $x_1 = 4.211$, $x_2 = 0$ for the central schemed cases B1 (−−), B3 (−.), B5 (−)

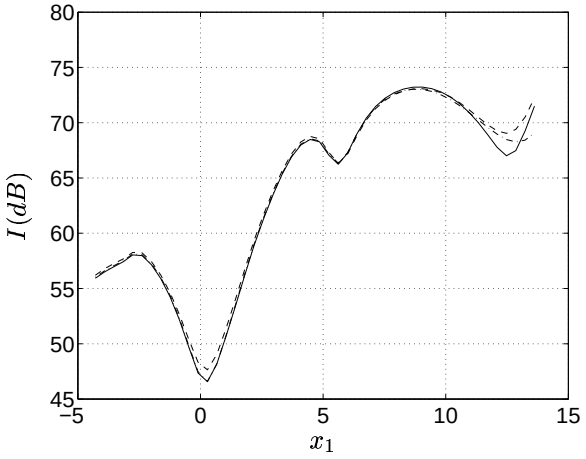

(c) Wall pressure intensities for the upwind schemed cases B2 (−−), B4 (−.), B6 (−)

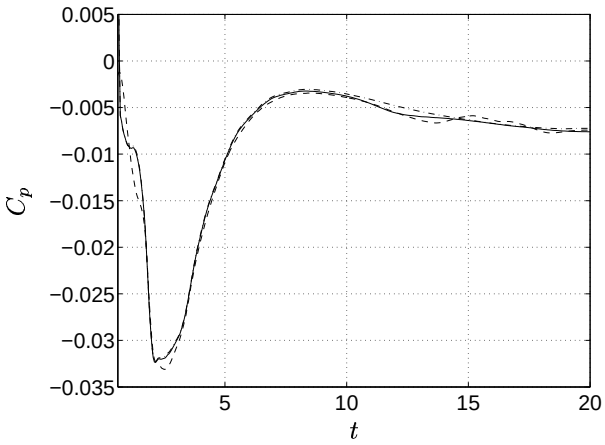

(d) Time series of C_p at $x_1 = 4.211$, $x_2 = 0$ for the upwind schemed cases B2 (−−), B4 (−.), B6 (−)

Figure 5. Results from the buffer-zone evaluation according to Table 2

B4 where only a small distortion still exist for the central scheme. Case B5 with $i = 1$ imposes too high a damping in the upstream region of the buffer-zone causing reflections into the domain. Due to the pressure drop in the buffer-zone the background pressure is increased compared to the boundary condition study. This increase is best showed in the latest part of the time series but is expected to have insignificant effect on the radiated noise due to its long time scale and slow variation. From these findings it is concluded that the most critical cases are the central schemed cases. Typically for these cases are a vortex intensity of $I_\omega \approx 0.165$ compared to $I_\omega \approx 0.145$ for the upwinded cases. Therefor, by designing the buffer zone with regard to the central schemed cases a sufficiently damping ratio will be obtained also for the upwind cases. Another conclusion drawn is that the parabolic shape is preferable due to its slower damping ratio in the

first part of the buffer-zone compared to a linear shape. A linear relation between the vortex intensity at the entrance plane of the buffer-zone and the required length of the buffer-zone is assumed, i.e.

$$\frac{I_{\omega}^{B3}}{L^{B3}} = \frac{I_{\omega}^{OC}}{L^{OC}} \tag{25}$$

In Eq. 25, superscripts B3 is the values found form case B3 and OC corresponds to the open cavity case. From this assumption a minimum required length of the open cavity buffer zone can be computed based on the findings from case B3 and the computed vortex intensity for the open cavity cases. This assumption requires that the vortex convection speed is approximately the same and that a linear assumption between different cases can be made.

V. Results from the open cavity case

The last part of the result section presents the open cavity case. The cases conducted in this section are presented in Table 3 together with the computed vortex intensity at the buffer-zone entrance plane. Given

Open cavity				
Case	NC/XB	Discretization scheme	Shape	$I_{\omega,max}$
C1	88/5.0	C	[2]	0.260
C2	88/5.0	VL	[2]	0.164

Table 3. Description of the open cavity cases together with the computed vortex intensity

the above conditions the flow oscillates in *Wake-mode*. This mode is characterized by violent ejections of vortices from the cavity with length scales comparable with the cavity dimensions rather than the thickness of the boundary layer. The ejected vortex admits the freestream fluid to hit the cavity downstream face and permits a new vortex to be generated close to the upstream cavity face. This vortex grows in the cavity until it almost fills the cavity and again gets ejected and triggers the next vortex shedding. In Fig. 6 the time history of the cavity drag is presented for cases C1 and C2. The contributing components to the drag force is the wall normal pressure over the upstream and downstream cavity walls and the friction contribution from the lower cavity wall. From Fig. 7 a comparison is made between the reference case and C2. As can be seen in Figs. 6 and 7 the ejection of the large vortex structures generates as expected rapid changes in the cavity drag. The lowest value occurs at the point when the vortex starts to get ejected out of the cavity causing a low pressure zone at the cavity downstream face Fig. 8(b). The maximum peak in the cavity drag occurs when the vortex partly has left the cavity and exposes the downstream cavity face to the freestream Fig. 8(e). The fundamental frequency between the reference case and the open cavity case are almost identical. C1 gives a $St_L = 0.245$ compared to $St_L = 0.243$ for the reference case. The fundamental frequency is defined as

$$St_L = \frac{fL}{U_{\infty}} \tag{26}$$

where L is the cavity length. In Figs. 8(a) to 8(f) six snapshots of the vorticity field are presented. Three major clockwise rotating vortices and one counter clockwise rotating vortex can be identified over the buffer-zone entrance plane, Fig. 8(a), Fig. 8(c) and Fig. 8(f). These are the structures that one primarily wants to damp out over the buffer-zone. In order to identify the strongest structure and estimate the parameter $I_{\omega,max}$ presented in Table 3 the time series of the vortex intensity is split into three windows treating each structure separately. The findings resulted in three values for the investigated parameter, $I_{\omega,1} \approx 0.14$, $I_{\omega,2} \approx 0.26$ and $I_{\omega,3} \approx 0.16$ which gives $I_{\omega,max} \approx 0.26$ for case C1. These are the results presented in Table 3 together with the findings from the other cases. The conclusion from Eq. 25 is then that the buffer-zone length is too short for C1 but should be sufficient for C2.

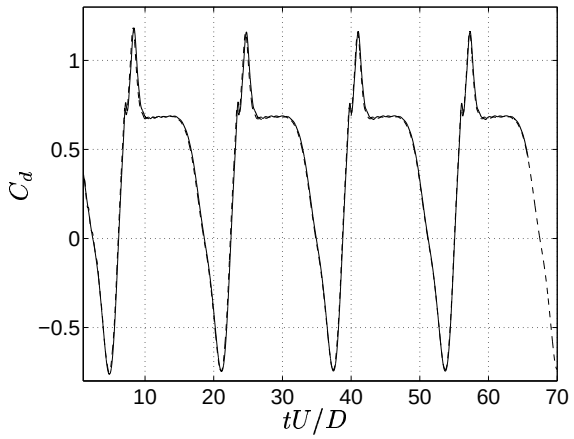

Figure 6. C_d **for cases, C1 (−−), C2 (−)**

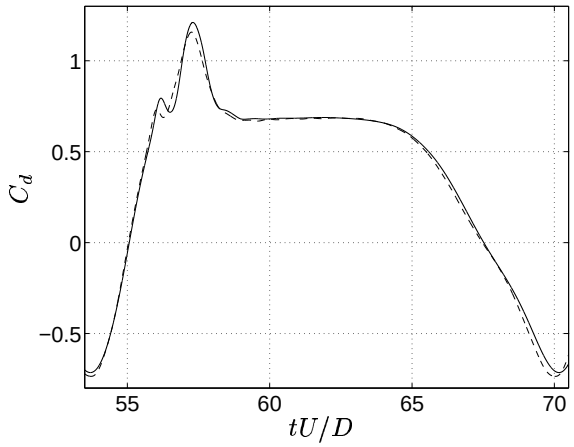

Figure 7. C_d **over one period, reference (−), C2 (−−)**

In Figs. 9 and 10 the wall source intensities for the reference case, C1 and C2 are presented. The geometry is fold out to visualize the results also over the two vertical walls. The source intensity is computed as

$$SPL = 20log_{10}\left(\frac{\phi_{l,rms}}{\phi_{l,ref}}\right) \tag{27}$$

where, $\phi_{l,ref} = \sqrt{\rho_\infty a_\infty 10^{-12}}$ and $\phi_{l,rms}$ is the rms value of the two treated source terms, respectively.

Over the cavity walls all cases show good agreement, but further downstream an over prediction of the intensity levels can be seen for both C1 and C2. At the inlet the imposed boundary condition is also causing an over-prediction for the incompressible cases. However, the levels at the inlet are relatively low compared to the levels downstream.

The second part of this analysis contains the results for the radiated sound where the observer locations are presented in Table 4. In Figs. 11(a) to 11(d) a successive surface integration is conducted in an attempt

Observers		
Observer	x_1	x_2
1	-2D	7.18D
2	-1D	7.18D
3	0D	7.18D
4	1D	7.18D
5	2D	7.18D
6	3D	7.18D
7	4D	7.18D
8	5D	7.18D
9	6D	7.18D

Table 4. Observer locations

to find where eventual discrepancies occur. Fig. 11(a) shows the sound directivity when integrating over the

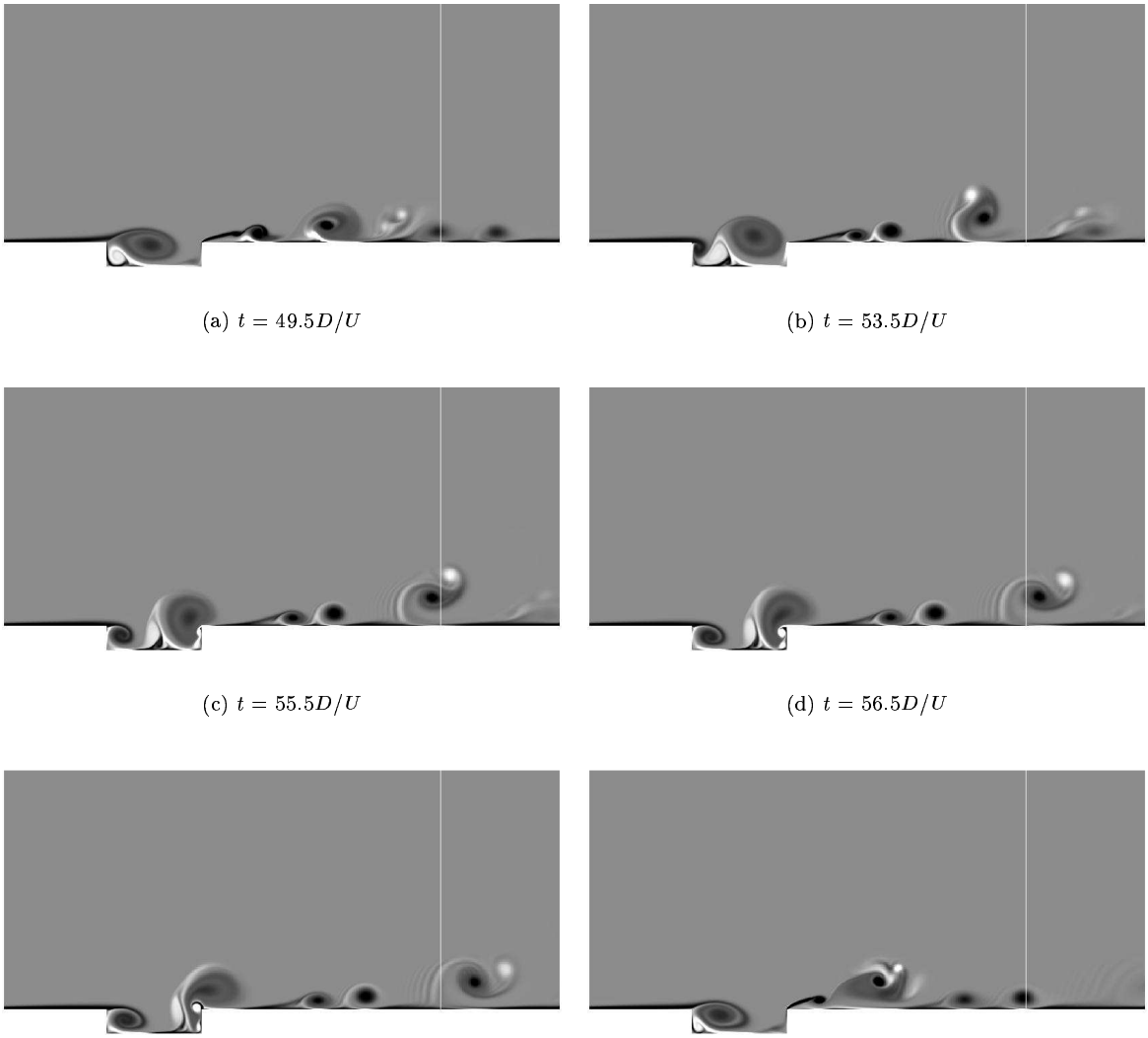

(a) $t = 49.5D/U$ (b) $t = 53.5D/U$

(c) $t = 55.5D/U$ (d) $t = 56.5D/U$

(e) $t = 57.5D/U$ (f) $t = 62.0D/U$

Figure 8. Snapshots of vorticity for case C1, $-2.5 < \Omega_z < 2.5$

cavity walls for the nine observers and an almost perfect match between the compared cases is observed. In the next figure, Fig. 11(b) the inlet wall is included in the surface integration and a small offset between the reference case and cases C1 and C2 can be found. The inlet wall tends to increase the sound levels over the cavity in contrast to the first part of the outlet wall presented in Fig. 11(c). From this figure it is clear that the first section of the outlet wall lowers the levels especially for the observers closest to the cavity trailing edge. The last figure Fig. 11(d) shows that the last part of the outlet wall gives positive contribution to the most downstream positioned observers. The positive contribution is much larger for the compressible case than for the the two incompressible cases which show an under prediction for the last observer. The surface integration extends here from the inlet to $10D$ downstream the cavity trailing edge where the buffer-zone starts for the incompressible cases.

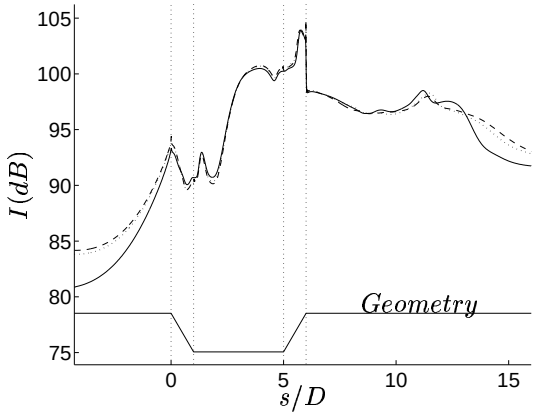

Figure 9. Wall source intensity for term 1, reference (-), C1 (..), C2 (- -)

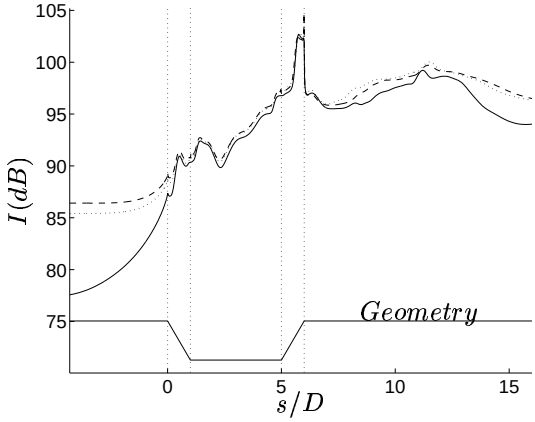

Figure 10. Wall source intensity for term 2, reference (-), C1 (..), C2 (- -)

VI. Conclusion

In this work two approaches are investigated to reduce reflections from the outlet boundary when strong vortices are present in the domain. Additionally, two second order discretization schemes are compared where the first is a central scheme and the second is the monotonic Van Leer scheme. Initially three outlet boundary conditions of convective type are investigated for a clock wise rotating vortex over a wall where the vortex is convected by a laminar velocity profile. The findings from this study show that large oscillations occurs when vortices are convected over the outlet boundary. To circumvent this problem a buffer-zone technique was investigated. The depending parameters were identified as the vortex intensity over the buffer-zone entrance plane, the buffer-zone length and the shape of the spatial damping ratio. Generally, the most important parameter regarding the buffer-zone is the time the vortex spends in the damping zone. This requires of course that the resolution in the zone is sufficiently smooth, which otherwise will result in impedance reflections into the domain. This technique was further investigated for the open cavity case. Results in terms of wall pressure intensities and radiated sound were then presented and compared against a previously work conducted in [4]. The findings show that even though the buffer-zone is located rather close to the cavity geometry acceptable sound levels can be obtained by an incompressible approach. By using this technique contamination of the background pressure due to the outlet boundary is minimized and the remaining discrepancies in wall source intensities and emitted noise are probably caused by compressible effects and mesh resolution. Another reason for the discrepancies is that in the compressible simulation a buffer-zone was used at the inlet. Regarding the different schemes used in the study one would expect lower noise levels from the upwind scheme due to its dissipative nature. The results show however small discrepancies between the two schemes and can be considered insignificant in terms of both the wall source intensities as well as for the emitted sound.

VII. Acknowledgments

This work was supported by Volvo Cars Corporation and the Swedish Agency for Innovation Systems (VINNOVA). I also would like to thank Johan Larsson who kindly let me use his database for the validation case and Dr. Billson for thoughtful discussions.

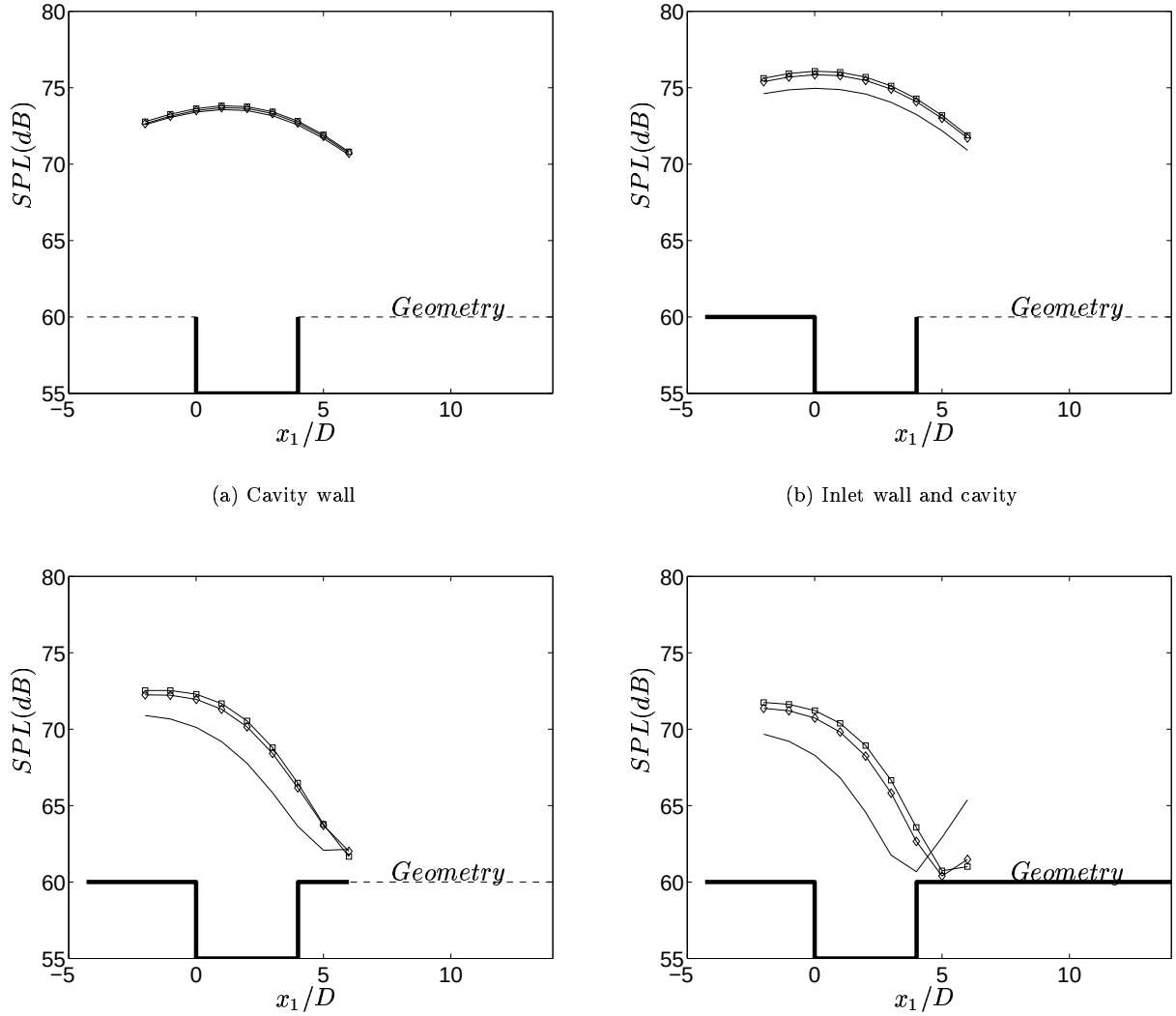

(a) Cavity wall

(b) Inlet wall and cavity

(c) Inlet wall, cavity and part of the outlet wall

(d) Entire wall

Figure 11. SPL when successively increasing the integration surface, Reference (-),C1 (⋄), C2 (□)

References

[1]Curle, N., "The influence of solid boundaries upon aerodynamic sound," *Proc. Roy. Soc*, Vol. A231, 1955, pp. 505–514.

[2]Leer, B., "Towards the Ultimate Conservative Difference Scheme II. Monotonicity and Conservation Combined in a Second-Order Scheme," *Journal of Computational Physics*, Vol. 14(4), 1974, pp. 361–370.

[3]Larsson, J., "Computational Aero Acoustics for Vehicle Applications," Chalmers University of Technology, 2002.

[4]Larsson, J., Davidson, L., Olsson, M., and Eriksson, L., "Aero acoustic investigation of an open cavity at low Mach number," *AIAA Journal*, Vol. 42(12), 2004, pp. 2462–2473.

[5]Rockwell, D. and Naudascher, E., "Review, Self-Sustained Oscillations of Flow Past Cavities," *Journal of Fluids Engineering*, Vol. 100, 1978, pp. 152–165.

[6]Gharib, M. and Roshko, A., "The effect of flow oscillations on cavity drag," *Journal of Fluid Mechanics*, Vol. 177, 1987, pp. 501–530.

[7]Colonius, T., Basu, A. J., and Rowley, C. W., "Computaion of sound generation and flow/acoustic instabilities in the flow past an open cavity," *3rd ASME/JSME Joint Fluids Engineering Conference*, 1999, pp. FEDSM99–7228.

[8]Rowley, C. W., Colonius, T., and Basu, A. J., "On self-sustained oscillations in two-dimensional compressible flow over rectangular cavities," *Journal of Fluid Mechanics*, Vol. 455, 2002, pp. 315–346.

[9]Ask, J. and Davidson, L., "An acoustic analogy applied to the laminar upstream flow over an open 2D cavity," *In press, C.R. Mecanique*, 2005.

[10]Lundbladh, A., Berlin, S., Skote, M., Hildings, C., Choi, J., Kim, J., and Henningson, D., "An Efficient Spectral Method for Simulation of Incompressible Flow over a Flat Plate," Technical report 1999:11, Dept. of Mechanics, Royal Institute of Technology, 1999.

[11]Davidson, L. and Farhanieh, B., "CALC-BFC, A Finite-Volume Code Employing Collocated Variable Arrangement and Cartesian Velocity Components for Computation of Fluid Flow and Heat Transfer in Complex Three-Dimensional Geometries," Chalmers University of Technology, Department of Thermo and Fluid Dynamics, 1995.

[12]Krajnović, S., *Large-Eddy Simulations for Computing the Flow Around Vehicles*, Ph.D. thesis, Chalmers University of Technology, 2002.

[13]Bredberg, J., *Turbulence Modelling for Internal Cooling of Gas-Turbine Blades*, Ph.D. thesis, Chalmers University of Technology, 2002.

[14]Dahlström, S., *Large Eddy Simulation of the Flow Around a High-Lift Airfoil*, Ph.D. thesis, Chalmers University of Technology, 2003.

[15]Nilsson, H., *Numerical Investigations of Turbulent Flow in Water Turbines*, Ph.D. thesis, Chalmers University of Technology, 2002.

[16]Hirsch, C., *Numerical Computation of Internal and External Flows*, John Wiley and Sons, 1991.

[17]Ffowcs Williams, J. and Hawkings, D., "Sound generation by turbulence and surfaces in arbitrary motion," *Philos. Trans. Roy. Soc.*, Vol. A 264 No. 1151, 1969, pp. 321–342.

[18]Brentner, K. and Farassat, F., "Modeling Aerodynamically Generated Sound of Helicopter Rotors," *Prog. Aerospace Sci.*, Vol. 39, 2003, pp. 83–120.